

---

# Optimizing Image Compression Ratio for Generating Highly Accurate Local Digital Terrain Models: Experimental Study for Martian Moons eXploration Mission

---

[Yuta Shimizu](#) , [Hideaki Miyamoto](#) <sup>\*</sup> , Shingo Kameda

Posted Date: 17 October 2023

doi: 10.20944/preprints202310.1027.v1

Keywords: Image compression; local DTM; Optimal compression ratio; SSIM; MMX



Preprints.org is a free multidiscipline platform providing preprint service that is dedicated to making early versions of research outputs permanently available and citable. Preprints posted at Preprints.org appear in Web of Science, Crossref, Google Scholar, Scilit, Europe PMC.

Copyright: This is an open access article distributed under the Creative Commons Attribution License which permits unrestricted use, distribution, and reproduction in any medium, provided the original work is properly cited.

Article

# Optimizing Image Compression Ratio for Generating Highly Accurate Local Digital Terrain Models: Experimental Study for Martian Moons eXploration Mission

Yuta Shimizu <sup>1</sup>, Hideaki Miyamoto <sup>1,\*</sup> and Shingo Kameda <sup>2</sup>

<sup>1</sup> Department of Systems Innovation, The University of Tokyo, Tokyo 1130033; shimizu@seed.um.u-tokyo.ac.jp (Y.S.), hm@sys.t.u-tokyo.ac.jp (H.M.)

<sup>2</sup> Department of Physics, Rikkyo University, Tokyo 1718501; kameda@rikkyo.ac.jp

\* Correspondence: hm@sys.t.u-tokyo.ac.jp; +81-3-5841-7027.

**Abstract:** Recent technological advances have significantly increased the data volume obtained from deep space exploration missions, making the downlink rate a primary limiting factor. Particularly, JAXA's Martian Moons eXploration (MMX) mission encounters this problem when identifying safe and scientifically valuable landing sites on Phobos using high-resolution images. A strategic approach in which we effectively reduce image data volumes without compromising essential scientific information is thus required. In this work, we investigate the influence of image data compression, especially as it concerns the accuracy of generating the local Digital Terrain Models (DTMs) that will be used to determine MMX's landing sites. We obtain simulated images of Phobos that are compressed using the CCSDS-120 with integer/float-point discrete wavelet transform (DWT), candidate algorithms for the MMX mission. Accordingly, we show that, if the compression ratio is 70% or lower, the effect of image compression remains constrained, and local DTMs can be generated within altitude errors of 40 cm on the surface of Phobos, which is ideal for selecting safe landing spots. We conclude that the compression ratio can be increased as high as 70%, and such compression enables us to facilitate critical phases in the MMX mission even with the limited downlink rate.

**Keywords:** image compression; local DTM; Optimal compression ratio; SSIM; MMX

## 1. Introduction

In-situ observations from robotic explorations, such as the Hayabusa [1], Hayabusa2 [2], Rosetta [3], and OSIRIS-REx (Origins, Spectral Interpretation, Resource Identification, Security, Regolith Explorer) [4] missions, have significantly contributed to expanding our understanding of the solar system. Subsequently, more deep space exploration missions are planned to be launched [5–8]. In these exploration missions, we can expect to obtain a large amount of scientific data relatively easily due to recent technological advances. However, the longer distances between spacecraft and the ground, coupled with limited transmission power constrained by several factors such as antenna size and power consumption, often result in significantly low downlink rates. Smart data-handling strategies must, in this regard, be considered within the constraints of limited downlink rates to maximize scientific returns from future deep space exploration missions.

The limited downlink speed can be one of the biggest issues for the Japan Aerospace Exploration Agency (JAXA)'s Martian Moons eXploration (MMX) mission, which is scheduled to be launched in 2024 [9]. Specifically, this mission will explore the moons of Mars, Phobos, and Deimos to determine their origins and evolutions. There are several theories on the formation mechanisms of the two moons. The basic parameters, such as their small sizes, low bulk densities, irregular shapes, and low albedos, and the visible to near-infrared reflectance spectra lead to the captured asteroid origin theory, where primitive carbonaceous chondrites originating at the outside of Mars' system could be captured by the Mars' gravity [10–12]. On the other hand, their orbital parameters, including the low orbital inclinations and eccentricities, and some numerical studies support the giant impact origin

theory, where ejecta materials could accrete and form the moons after a giant impact on Mars [13–19].

To conclude this discussion about the origins, the MMX mission is planned to perform landings on Phobos (ideally two times on different sites) and collect surface materials ( $\geq 10$  g), which will be returned to Earth in 2029 and analyzed in laboratories [9]. Although previous missions such as Hayabusa [1], Hayabusa2 [2], and OSIRIS-REx [4] missions performed touchdowns (instant contacts on the surfaces within a second) and collected samples from the surfaces of asteroids, the landing and sampling in MMX mission have become more challenging in that the spacecraft will have to safely land and stay for approximately 2.5 hours on Phobos [20], where knowledge of the surface is limited. Nevertheless, Phobos is expected to contain plenty of topographic irregularities including slopes [21], craters [22–27], rock particles (i.e., boulders, cobbles and pebbles) [28], and grooves [23,24,28–31]. The gravity of Phobos ( $\sim 1/2000$  G [32]) is also relatively higher than on any other small asteroids on which touchdowns were previously performed ( $\sim 1/10^5 - 1/10^4$  G [33–37]), so the landing site selection could be one of the most crucial phases for this mission.

Based on the current specifications of MMX spacecraft, we need to find flat regions with altitude differences smaller than 40 cm [38]. Although previous missions, such as Mariner-9 [39], Viking-Orbiter [40], Mars Global Surveyor [28], Mars Express [41], Mars Reconnaissance Orbiter [42], and Emirates Mars mission [43] have observed Phobos and Deimos thus far, the resolutions of obtained optical images and three-dimensional shape models are insufficient considering this severe requirement for the landing sites. While some numerical studies have indicated the capability of finding smooth enough regions for the landing on Phobos [38], if we establish the safety of the spacecraft during landing as the ultimate priority, then the most practical strategy is performing in-situ observations after the arrival and finding safe regions for the landings.

The MMX spacecraft is thus equipped with two optical cameras: the Telescopic Nadir Imager for GeOmOrphology (TENGOO) and the Optical RadiOmeter Composed of CHromatic Imagers (OROCHI) [44]. The high-resolution image capabilities of these cameras are critical for landing-site selection. To map Phobos's surface with a resolution of  $\sim 12$  cm/pix from a quasi-satellite orbit (QSO) around the moon, the cameras have been designed to exhibit superior performance in comparison to optical cameras on previous sample-return missions, such as AMICA of Hayabusa [45], ONC-T of Hayabusa2 [46], and OCAMS of OSIRIS-REx [47] missions. With a  $3296 \times 2472$  pixel image size and a 16-bit depth, these specifications are significantly advantageous for minutely observing Phobos's surface. However, this increased resolution results in a substantial image file size growth, with raw images potentially reaching 16.3 MB. Transmitting such large images to the ground could require over 1.1 hours when utilizing the MMX's typical telecommunication system with a speed of  $\sim 32$  Kbps. This downlink duration is not practical given the limited observational period of the landing-site selection, which is scheduled to be performed within approximately half a year and is severely constrained by illumination conditions determined by the relative positions of the spacecraft, Phobos, Mars, and sun [20]. Additionally, the precise sample collection locations must be determined within the brief 2.5-hour landing window, allowing under 1 hour for downlinks.

One reasonable operation for transmitting such image data is to utilize data compression techniques, with numerous lossy compression algorithms that have been developed to reduce image file sizes significantly. Nonetheless, highly compressed images can become distorted and scientifically unusable. Optimizing image data handling, which will ensure data volume reduction without compromising scientific value, is, therefore, significant for future deep space exploration missions, including the MMX mission. While previous studies have analyzed the influence of data compression on images of exploration missions [48,49], to fulfill the requirements of the landing operations of the MMX mission, we mainly focus on the effect of image compression on the accuracy of local DTM generation to show whether such compressions lose any critical information necessary for selecting safe landing sites on Phobos (i.e.,  $\sim 40$  cm altitude differences).

## 2. Materials and Methods

### 2.1. Experimental setup

Although previous studies showed the existence of various geological characteristics on Phobos, including craters, grooves, and boulders [23,24,28], the spatial resolutions of the images obtained by previous exploration missions are limited (lower than several meters per pixel), and the detail of the roughness is still unknown [38]. This knowledge gap will remain until the MMX spacecraft arrives at Phobos and reveals detailed surface structures through high-resolution images. Accordingly, we prepare simulated images of Phobos with both rough and smooth surfaces to accurately evaluate the influence of image compression on the selection of landing sites under various surface conditions of Phobos.

For the simulated images of a rough surface, we use the simulator for the OROCHI, an optical chromatic imager onboard the MMX spacecraft [44]. This OROCHI simulator has seven wide-angle bandpass imagers, with a pixel pitch of  $5.86 \mu\text{m}$  and a focal length of 12.5 mm, achieving the iFoV of 0.469 mrad/pix that is similar to the iFoV of the OROCHI (0.44-0.46 mrad/pix [44]). The seven band-pass filters have wavelengths of 390 nm, 480 nm, 550 nm, 650 nm, 700 nm, 800 nm, and 950 nm, respectively (Figure 1a). Furthermore, these imagers are mounted on an aluminum frame and can operate simultaneously, allowing the camera to capture the same region on the Phobos surface in seven different colors, which is useful for determining suitable landing sites and identifying the uniformity or nonuniformity of the distribution of surface materials. In this study, we mainly focus on images obtained by the imager with the band-pass filter having the wavelength of 550 nm, a wavelength commonly used in previous exploration missions, including Hayabusa and Hayabusa2 missions [45,46]. For the surface material, we used University of Tokyo Phobos Simulant, Tagish Lake Based (UTPS-TB) [50]. This simulated Phobos regolith material is developed and processed using terrestrial soils and materials, exhibiting a reflectance spectrum similar to that of Phobos surface materials, which allows for the acquisition of images that closely resemble those anticipated from the MMX mission.

The images were obtained with the following experimental setup (Figure 1b). UTPS-TB was spread over a foundation with a size of approximately  $60 \times 120$  cm. The OROCHI simulator was fixed to a frame to prevent image blurring due to camera shake. This frame can be moved to capture images from different regions using the same imager. Images were taken from a height of approximately 70 cm directly above the foundation. A halogen lamp, whose wavelength domain is not covered by the seven band-pass filters, served as the light source, with an incidence angle (phase angle) of  $30^\circ$ , an optimal angle for observing surface rocks. Each image has a size of  $1920 \times 1200$  pixels. Note that TENGGO and OROCHI use a 14-bit A/D converter, while data is stored with a bit depth of 16 bits. To simulate this data structure, we converted 8-bit color images from the OROCHI simulator to 16-bit grayscale images, ensuring that each pixel value fell within the 14-bit depth range. Also, the OROCHI simulator images contained a dark surrounding frame due to the band-pass filters, which we excluded in the post-processing, as explained in Section 2.3.

With a similar procedure, we obtained simulated images of Phobos with a smooth surface (Figure 1c). In this experiment, we used a digital camera commercially available to simulate the same image size as OROCHI and TENGGO ( $3296 \times 2472$  pixels). We used a foundation with a size of  $75 \times 150$  cm having circular depressions, which simulate craters on Phobos. Also, we spread UTPS-TB over the foundation as a surface material. Images were obtained from a height of approximately 188 cm above the foundation. As for the procedure of the simulated images for the smooth surface, we converted 16-bit color images to 16-bit grayscale images to simulate the condition of the TENGGO and OROCHI.

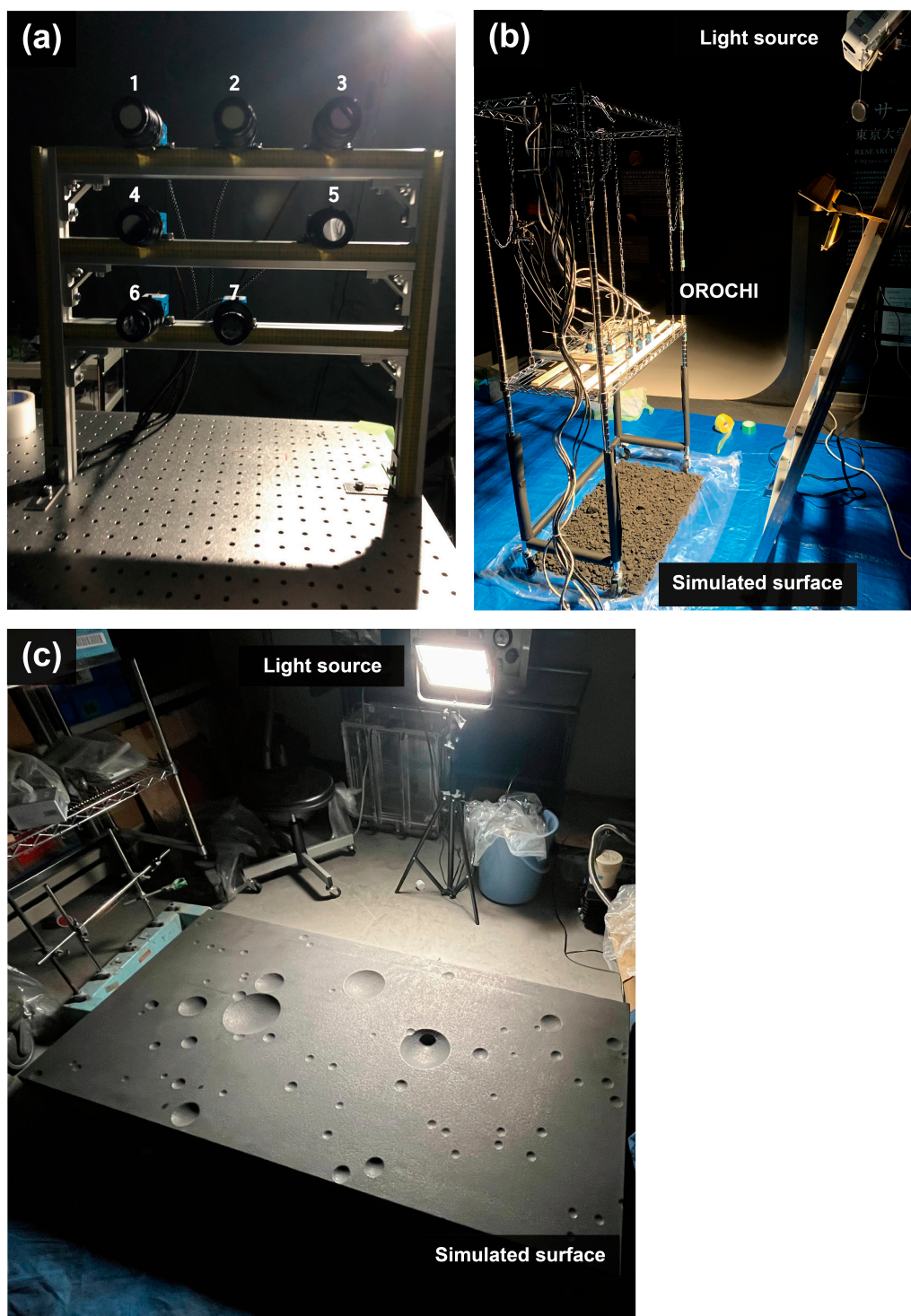


**Figure 1.** OROCHI simulator and experimental setups. (a) OROCHI simulator. Each number represents an imager with the corresponding band-pass filters: 1: 390 nm, 2: 480 nm, 3: 550 nm, 4: 650 nm, 5: 700 nm, 6: 800 nm, 7: 950 nm. (b) Experimental setup for simulated Phobos images with a rough surface. The OROCHI simulator model is fixed to a movable frame, enabling the capture of images of the same region from different camera positions. (c) Experimental setup for simulated Phobos images with a smooth surface. For a simulated surface, we use a foundation with circular depressions, resembling the actual cratered Phobos surface.

## 2.2. Image compression and image quality assessment

Image compression algorithms commonly perform two compression schemes: lossless and lossy compressions. In lossless compression, the original image data can be fully reproduced, while the compression ratio is substantially low (i.e., high data volume of a resulting product). Conversely, in lossy compression, the original image data cannot be fully recovered, but the compression ratio can be significantly high (i.e., low data volume of a resulting product). Considering the limited downlink rate of deep-space exploration missions, including the MMX mission, low data volume of a resulting product is important, and thus, we mainly focus on the image-handling strategies using lossy compression.

The image compression algorithm, CCSDS 120.0-B-1 (hereafter simply referred to as CCSDS-120), is specialized for use in spacecraft and is a candidate algorithm that will be used in the MMX mission. Because the complexity of this algorithm is sufficiently low, the processing speed during image handling can be sufficiently high even with hardware onboard spacecraft. CCSDS-120 uses the discrete wavelet transform (DWT) in the compression scheme, and it especially supports two different types of DWT: integer-point DWT and float-point DWT. The integer-point DWT compression process is for lossless compression; it requires only integer arithmetic with lower implementation complexity, but it can also be used in lossy compression. On the other hand, the float-point DWT provides improved compression speed at low bit rates but requires floating-point calculations and cannot provide lossless compression. This study examines both algorithms using integer and float points to determine the best compression scheme.

In practice, we used a public script published by the University of Nebraska (<http://hyperspectral.unl.edu/download.htm>) for image compression using CCSDS-120. Note that the compression ratio  $p$  in this study is defined as follows:

$$p = \left(1 - \frac{S_{\text{comp.}}}{S_{\text{org.}}}\right) \times 100 [\%], \quad (1)$$

where  $S_{\text{org.}}$  and  $S_{\text{comp.}}$  are the file sizes of compressed and original images, respectively.

For the evaluation metric to assess the influence of image compression on image quality, we use Structural SIMilarity (SSIM), one of the most widely used image quality indices [51]. Essentially, the SSIM evaluates image quality based on three comparisons: luminance, contrast, and structure comparisons. SSIM values range from 0.0 to 1.0, where a higher value indicates better image quality. A value of 1.0 shows that a given image is identical to the original image.

### 2.3. Generation of local DTMs

Structure from Motion (SfM) is one of the most famous and widely used algorithms to generate three-dimensional shape models from images obtained by satellites, drones, and spacecraft, for instance. The planetary science domain has utilized SfM in addition to several other conventional techniques, such as aerial photogrammetric approaches based on stereo-pairs [52], and small digital topography/albedo maps (L-map) determined from multiple images with stereophotoclinometry (SPC) [53]. A recent study revealed that the SfM's accuracy is compatible with SPC [54]. In the MMX mission, SfM is considered a reasonable algorithm for generating local Digital Terrain Models (DTMs). Thus, we use SfM to generate local DTMs.

In practice, we utilized Metashape Pro (ver. 1.6.4), a commercial software program for generating three-dimensional shape models. Leveraging high-end CPUs and GPUs (CPU of Core-i9 12900K and dual GPUs of GeForce RTX 3090), we reduced calculation times. We then explored optimal parameters for obtaining high-precision local DTMs, as shown in Table 1. Local DTMs were created with Metashape through the following processes:

1. Import images and image masks (i.e., binary images determining the processing areas) and set camera parameters (e.g., focal length and sensor pixel sizes).
2. Georeference cameras by importing camera coordinate files, which define positions (coordinates) and orientations (directions) for each camera.
3. Perform key-point matching by identifying distinctive features in images that can be recognized in other images and matching the most prominent features across the image dataset.

4. Perform bundle adjustment for three-dimensional geometry reconstruction using the network of matched features, incrementally adding images to update camera model parameters (e.g., focal length, radial distortion parameters) and camera orientations (i.e., positions, directions), and calculating three-dimensional coordinates for key points.
5. Generate a sparse point cloud representing the three-dimensional coordinates of the most prominent features in the image dataset, realign images with large coordinate errors, and remove outliers by observing the point cloud from various directions.
6. Build a dense point cloud by calculating depth and color information for each camera.
7. Generate polygon meshes from the dense point cloud that express detailed topography of the target shape.
8. Generate image masks by selecting areas on the mesh with high confidence, created from many points in the dense point cloud. Using those image masks, regenerate the model.
9. Generate the model's texture by combining the original images seamlessly with the reconstructed polygon meshes.

**Table 1.** Parameters used to generate local DTMs with high accuracy using Metashape.

Process	Parameter	Setting	Comments
Align photos	Accuracy	Highest	The program aligns photos with the highest accuracy.
	Generic preselection	On	The program makes low-resolution images and finds key points in order to decrease the process time.
	Reference preselection	On	The program generates sparse point cloud by using the camera coordinates information input a priori.
	Key point limit	0	Key points will be generated without the limitation of the number of points.
	Tie point limit	0	Tie points will be generated without the limitation of the number of points.
	Adaptive camera model fitting	Off	When this parameter is set to be On, the camera parameters for fitting the distortion of the lenses will be determined, which is not necessary in this research.
Build dense cloud	Accuracy	Ultra high	The dense cloud is generated with the highest accuracy.
	Depth filtering	Mild	How aggressively the program filters outliers obtained from the depth computation. "Mild" is recommended.
Build mesh	Surface type	Arbitrary (3D)	"Arbitrary (3D)" means that the program generates a closed 3D shape model without any holes.
	Source	Depth maps	The program generates the mesh using all the information from the input images including assumed depth maps, which is recommended to use.
	Quality	Ultra high	The mesh is generated with the highest accuracy.
	Face count	100,000,000	We set the parameter large enough in order to generate meshes without any limitations of the number or meshes.

Note that, to generate local DTMs with high quality, the amount of overlapping area in each image with other images is important. This scenario occurs because the large overlapping area leads to many reconstructed point clouds, resulting in a better quality of local DTMs. Thus, we first created models without any image masks (by Step 7). Then, we selected an area on each model where a large

number of point clouds are reconstructed and generated image masks. Using these masks, we processed only portions in each image with large overlaps with others and improved the quality of local DTMs (Step 8).

### 3. Results

#### 3.1. Phobos simulated images and local DTMs

Figures 2 and 3 show examples of the simulated images of Phobos with rough and smooth surfaces, respectively. Using the experimental setup with the rough surface, we obtained 10 images. The spatial resolution of these images is 0.379 mm/pix. On the other hand, by utilizing the experimental setup with the smooth surface, we acquired 44 images at a spatial resolution of 0.112 mm/pix.

Using these simulated images, we generated local DTMs for both rough and smooth surfaces (Figure 4). For the rough surface model, we created a dense point cloud composed of 3,826,280 points, resulting in a mesh with 2,309,668 facets. The standard deviation of the elevation is 19.2 mm. On the other hand, for the smooth surface model, we generated a dense point cloud containing 13,265,901 points, resulting in a mesh with 10,012,252 facets. The standard deviation of the elevation is 8.99 mm, which is smaller than that of the rough surface model and indicates this model's smoothness. In this manner, we generated local DTMs having a substantially large number of facets, which are compatible with models that will be generated in the MMX mission.

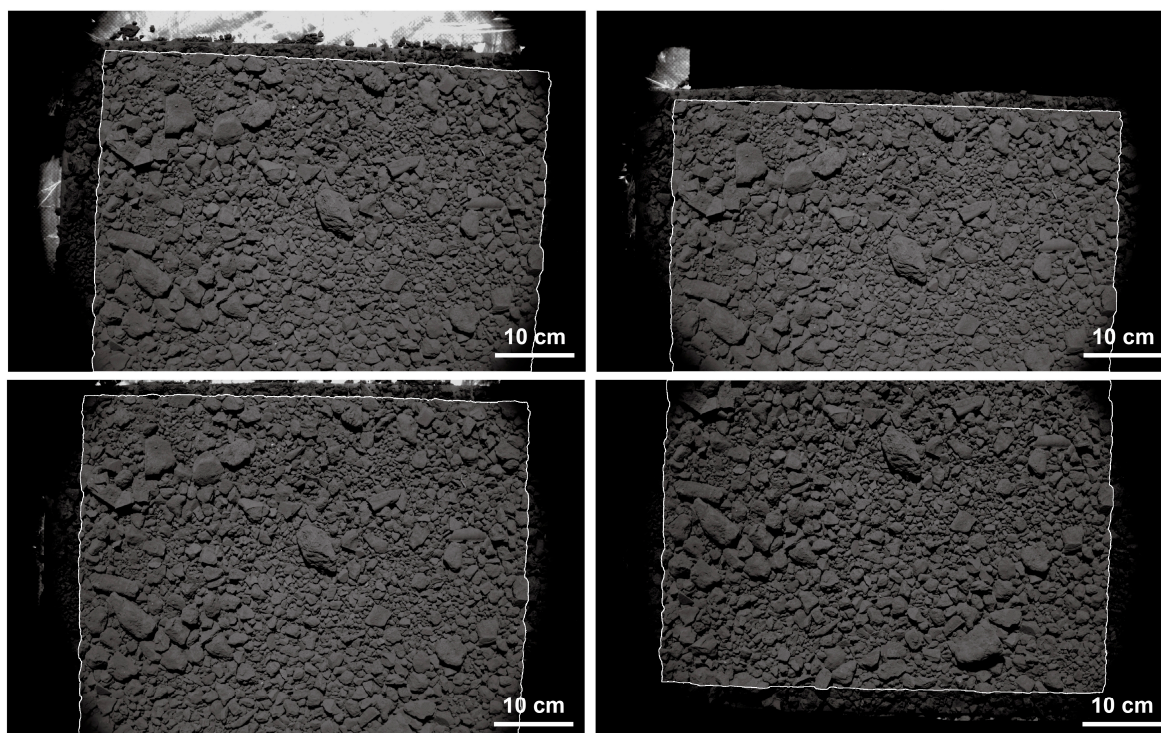


**Figure 2.** Examples of the simulated images for the rough surface. The image size is  $1920 \times 1200$  pixels and the color space is grayscale. The spatial resolution is 0.379 mm/pix. Note that dark regions surrounded by white lines represent image masks, which show ignored regions while generating the local DTMs. A total of 10 simulated images were prepared for the rough surface.

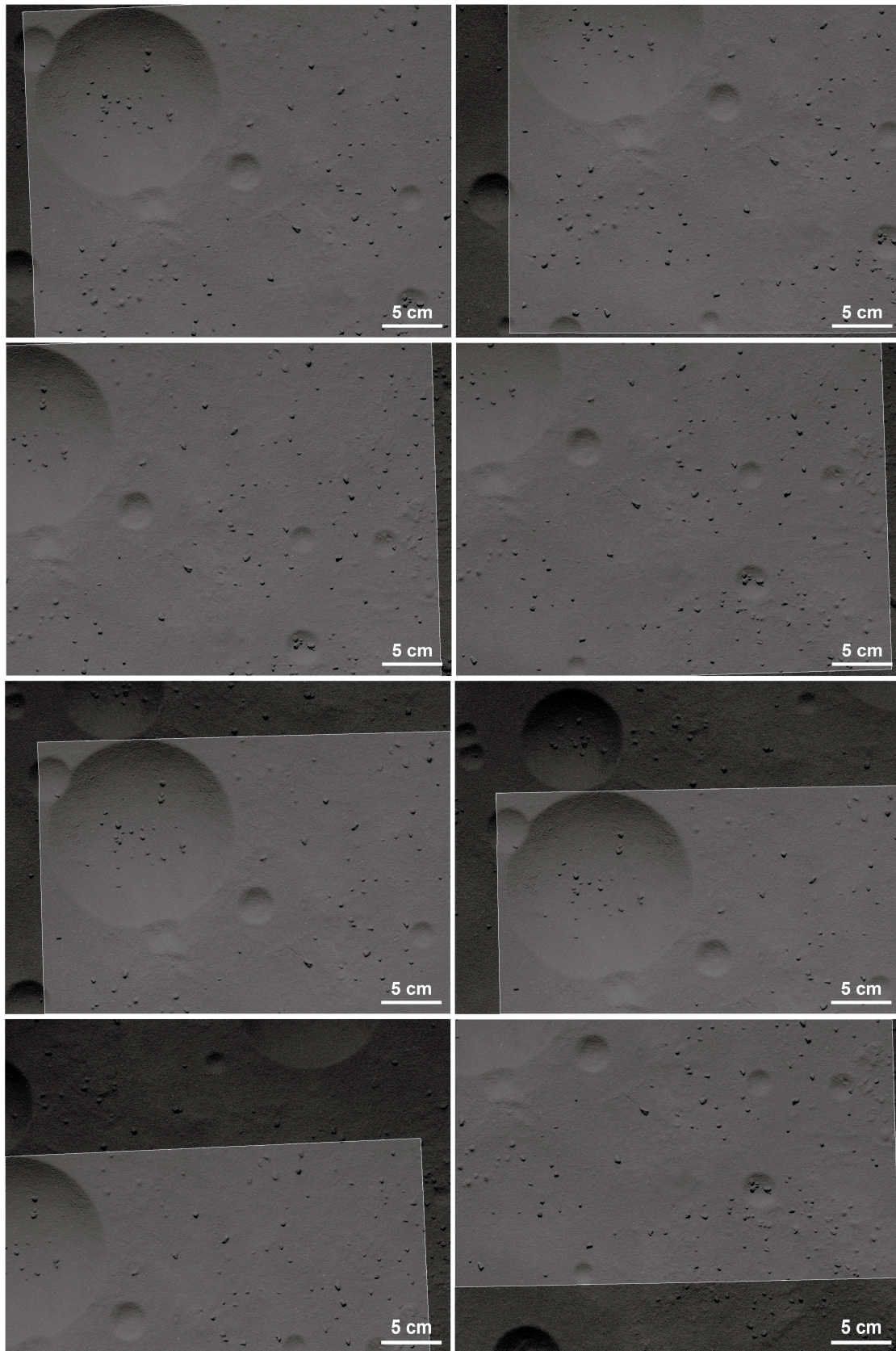


**Figure 3.** Examples of the simulated images for the smooth surface. The image size is  $3296 \times 2472$  pixels, and they are expressed in grayscale. The average spatial resolution is  $0.112 \text{ mm/pix}$ . Dark regions represent image masks, which show ignored regions while generating the local DTMs. A total of 44 simulated images were prepared for the smooth surface.

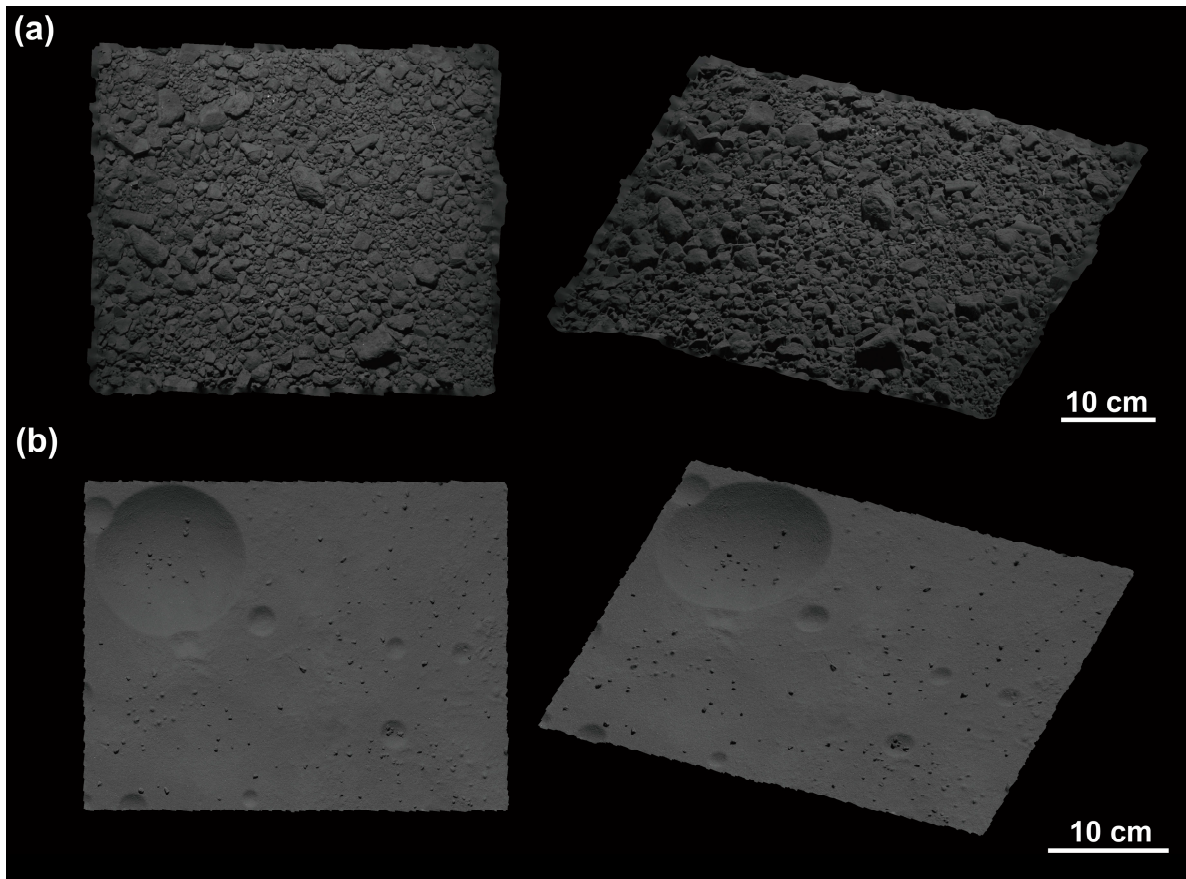


**Figure 4.** Local DTMs of the rough and smooth surfaces (a) Local DTM for the rough surface. The model is composed of 3,826,280 points and 2,309,668 facets. (b) Local DTM for the smooth surface. The model has 13,265,901 points, resulting in 10,012,252 facets. Those two models express simulated surfaces in a three-dimensional space with a substantially high resolution.

### 3.2. Influence of image compressions

We compressed the simulated images of the rough and smooth surfaces employing different compression ratios using the CCSDS-120 with float- and integer-point DWT (Figures 5 and 6). The processing speed of the CCSDS-120 with float-point DWT was approximately twice as fast as that of the integer-point DWT. Moreover, the difference in image compression performance between the two algorithms is limited, and visual changes or distortions in both simulated images of the rough and smooth surfaces are not distinctly noticeable until the compression ratio reaches 98%.

The image quality evaluation performed using SSIM also demonstrates that the difference in distortion levels between CCSDS-120 with float- and integer-point DWT is considerably limited (Figure 7). However, our quantitative analysis reveals that image quality can decrease at varying rates as the compression ratio increases depending on the surface characteristics depicted in the images (i.e., rough vs. smooth surfaces). Our result shows that simulated images of the smooth surface can be significantly affected by image compression even at lower compression ratios, whereas simulated images of the rough surface exhibit fewer distortions even at higher compression ratios. Likewise, this result reflects the data processing performed using DWT.

Images inherently consist of both high-frequency and low-frequency structures. High-frequency structures correspond to details and textures in images, while lower-frequency structures represent broader and more gradual changes in an image, such as variations in brightness. In the CCSDS with the DWT, the wavelet coefficients representing the high-frequency structures are more aggressively quantized or truncated, especially at higher compression ratios. Consequently, these high-frequency components are more susceptible to distortion than the low-frequency ones. Figures 5 and 6 also

show this effect, where small topographic features and textures, which constitute the highest-frequency structures in our images, are highly distorted by image compression. Essentially, the simulated images for the smooth surface contain more information related to such small topographic features (high-frequency structures) compared to the simulated images for the rough surface. This ratio means the former is more susceptible to image compression at the same compression ratio.

Across all images, quality loss remains constrained when the compression ratio is 70% or lower. With such compression ratios, we expect significant scientific information to be maintained. Therefore, we recommend compression ratios of 70% or lower to reduce the data volume and simultaneously retain important scientific information.

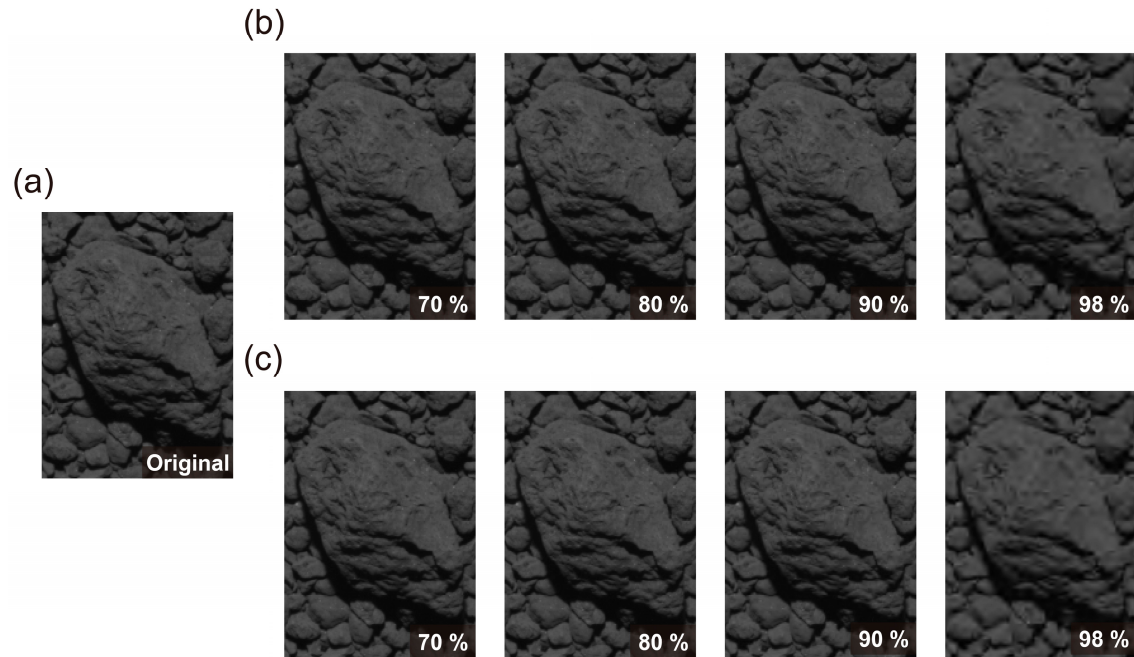


**Figure 5.** Image compression effects on the simulated image of the rough surface. (a) Original image. (b) Images compressed with CCSDS-120 with float-point DWT. (c) Images compressed with CCSDS-120 with integer-point DWT. The difference in the distortion level of the two different compression algorithms is minimal. From this simple visual analysis, distortions caused by image compression are not readily apparent until the compression ratio reaches 98%. Those distortions are basically found on small roughness or textures, which correspond to high-frequency structures in image processing using DWT.

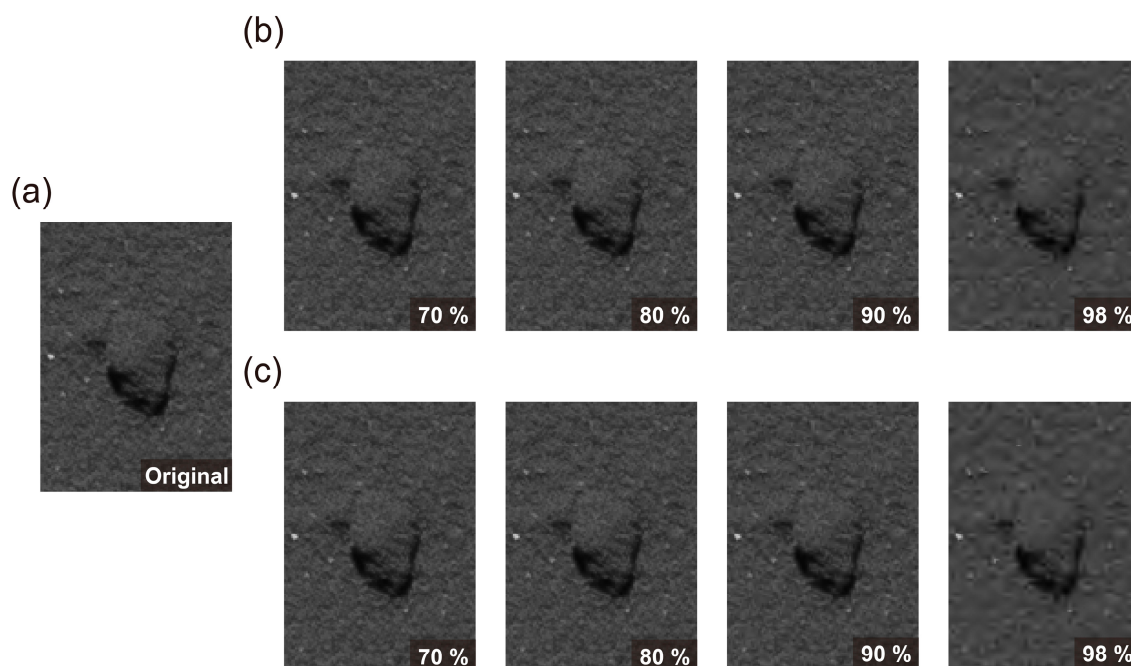


**Figure 6.** Image compression effects on the simulated image of the smooth surface. (a) Original image. (b) Images compressed with CCSDS-120 with float-point DWT. (c) Images compressed with CCSDS-120 with integer-point DWT. The difference in the distortion level of the two different compression algorithms is limited. Also, from this simple visual analysis, image distortion caused by compression cannot be confirmed clearly until the compression ratio reaches 98%. Such distortions, overall, exist in small roughness or textures, which correspond to high-frequency structures in the image-processing using DWT.

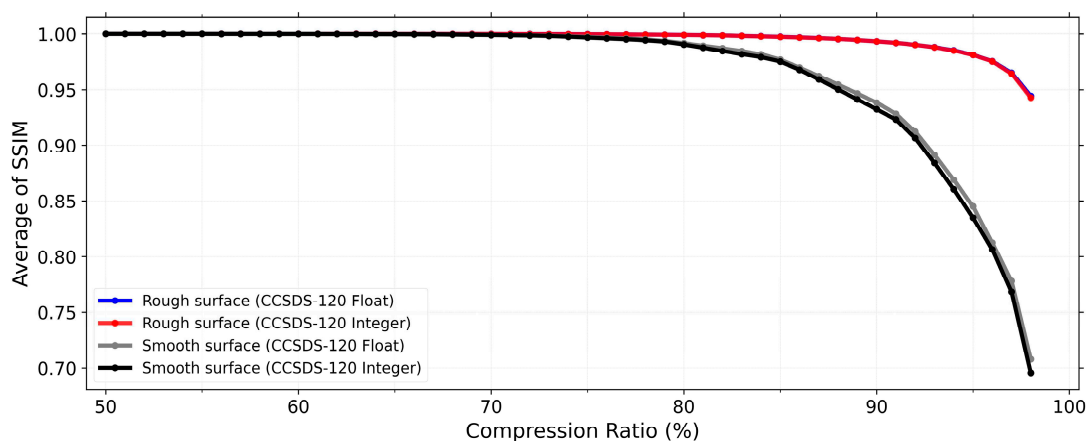


**Figure 7.** Image quality assessment using SSIM. The difference in the image quality decrease between CCSDS-120 with float- and integer-point DWT is consistently minimal across all compression ratios. Our quantitative analysis shows that the quality of simulated images for the smooth surface is more susceptible to image compression, even at lower compression ratios, compared to those for the rough surface. This result represents the characteristic of image-processing using DWT, where small roughness or textures (high-frequency structures) are more affected by image compression. Furthermore, we reveal that compression ratios equal to or lower than 70% exhibit limited loss of image quality.

#### 4. Discussion

#### 4.1. Effect of image compression on the accuracy of generating local DTMs

With a compression ratio of 70%, we analyze whether local DTMs contain critical errors (that is, over 40-cm altitude errors) to find safe landing sites for the MMX mission. We compare local DTMs generated from compressed images (compressed model) with the model generated from uncompressed images (original model). The error calculations are performed using CloudCompare (ver. 2.11.2), a public 3D point-cloud and mesh-processing software. In the model comparison, we first accurately registered the dense point cloud of the compressed models to that of the original model by minimizing the distances between each point. Then, we computed those distances and recorded them as errors.

Figure 8 shows the compressed model for the rough surface, generated by 70%-compressed images using CCSDS-120 with float- and integer-point DWT. The models are each generated within a 2% difference in the number of dense points and meshes from the original model. Figure 9 represents the result of the smooth surface, with models generated with 3% differences in the number of dense points and meshes compared to those of the original. These results show that the qualities of the model generated are maintained, even when we use 70%-compressed images.

Figures 8 and 9 also show the errors of the compressed models from the original models. We show that the compressed models for the rough surface can be generated with the errors of  $0.210 \pm 0.145$  mm (CCSDS-120 with float-point DWT) and  $0.208 \pm 0.146$  mm (CCSDS-120 integer-point DWT), respectively. For the smooth surface, however, we can generate the models with the errors of  $0.205 \pm 0.147$  mm (CCSDS-120 with float-point DWT) and  $0.200 \pm 0.145$  mm (CCSDS-120 integer-point DWT), respectively. In particular, the side with tall rock-particles or the floors of the circular depressions tend to exhibit greater errors (partly due to inadequate imaging), resulting in a reduced number of dense points generated by the SfM.

In the MMX mission, the equatorial region (i.e., latitude  $\leq 30^\circ$ ) of Phobos is planned to be primarily observed from the orbit named at QSO, which is approximately 20 km away from the surface, to reveal detailed topography and surface compositions and identify the best landing sites. Assuming the spacecraft typically obtains images with a resolution of  $\sim 12$  cm/pixel using the TENGGOO [20], which is sufficient to observe  $>20$  cm-sized hazardous rock particles, and scaling our image up, the 1 mm errors in our analysis can be equivalent to  $\sim 31.7$  cm errors for the rough surface and  $\sim 107$  cm errors for the smooth surface on Phobos. These errors are based on our image resolutions of 0.379 mm/pixel for the rough surface and 0.112 mm/pix for the smooth surface. In this case, for the rough surface, the errors are equivalent to  $6.66 \pm 4.60$  cm (CCSDS-120 with float-point DWT) and  $6.59 \pm 4.63$  cm (CCSDS-120 integer-point DWT), respectively. On the other hand, for the smooth surface, the errors are equivalent to  $21.9 \pm 15.7$  cm (CCSDS-120 with float-point DWT) and  $21.4 \pm 15.5$  cm (CCSDS-120 with integer-point DWT), respectively. This result means that local DTMs generated from compressed images with the compression ratio lower than 70% are expected not to include the error of the altitude larger than 40 cm, regardless of the surface roughness on Phobos. This situation is ideal for determining safe landing and sampling sites on the surface of Phobos. Therefore, we can expect that the compression ratio can be increased as high as 70% in the MMX mission, ensuring the safety of the spacecraft.

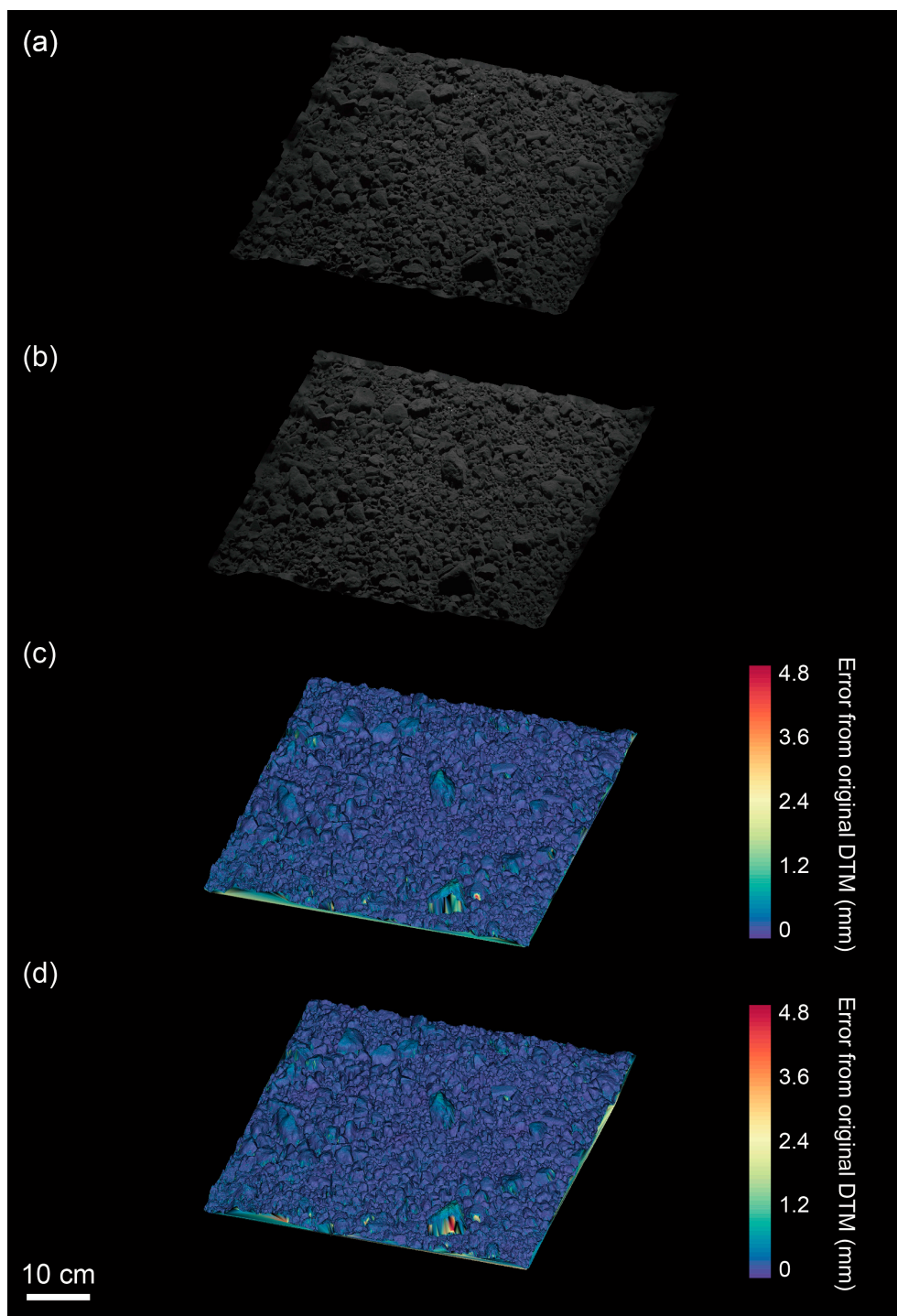


**Figure 8.** Compressed models for the rough surface and their error analysis. The error analysis shows the error of compressed models from the original models. **(a)** Local DTM generated by using compressed images processed by CCSDS-120 with float-point DWT. The model is composed of 3,872,302 dense points and 2,317,660 meshes. **(b)** Local DTM generated by using compressed images processed by CCSDS-120 with integer-point DWT. The model is composed of 3,873,461 dense points and 2,303,035 meshes. **(c)** The error analysis of the model shown in (a). The error of this model is  $0.210 \pm 0.145$  mm, equivalent to the error of  $6.66 \pm 4.60$  cm on Phobos. **(d)** The error analysis of the model shown in (b). The error of this model is  $0.208 \pm 0.146$  mm, equivalent to the error of  $6.59 \pm 4.63$  cm on Phobos. Both analyses show that the compressed models can be generated within 2% error of the number of dense points and meshes from the original model. Further, the altitude errors

can be smaller than 40 cm on Phobos, which means that 70% compressed images effectively reduce file sizes without losing important scientific information, especially for determining safe landing sites.

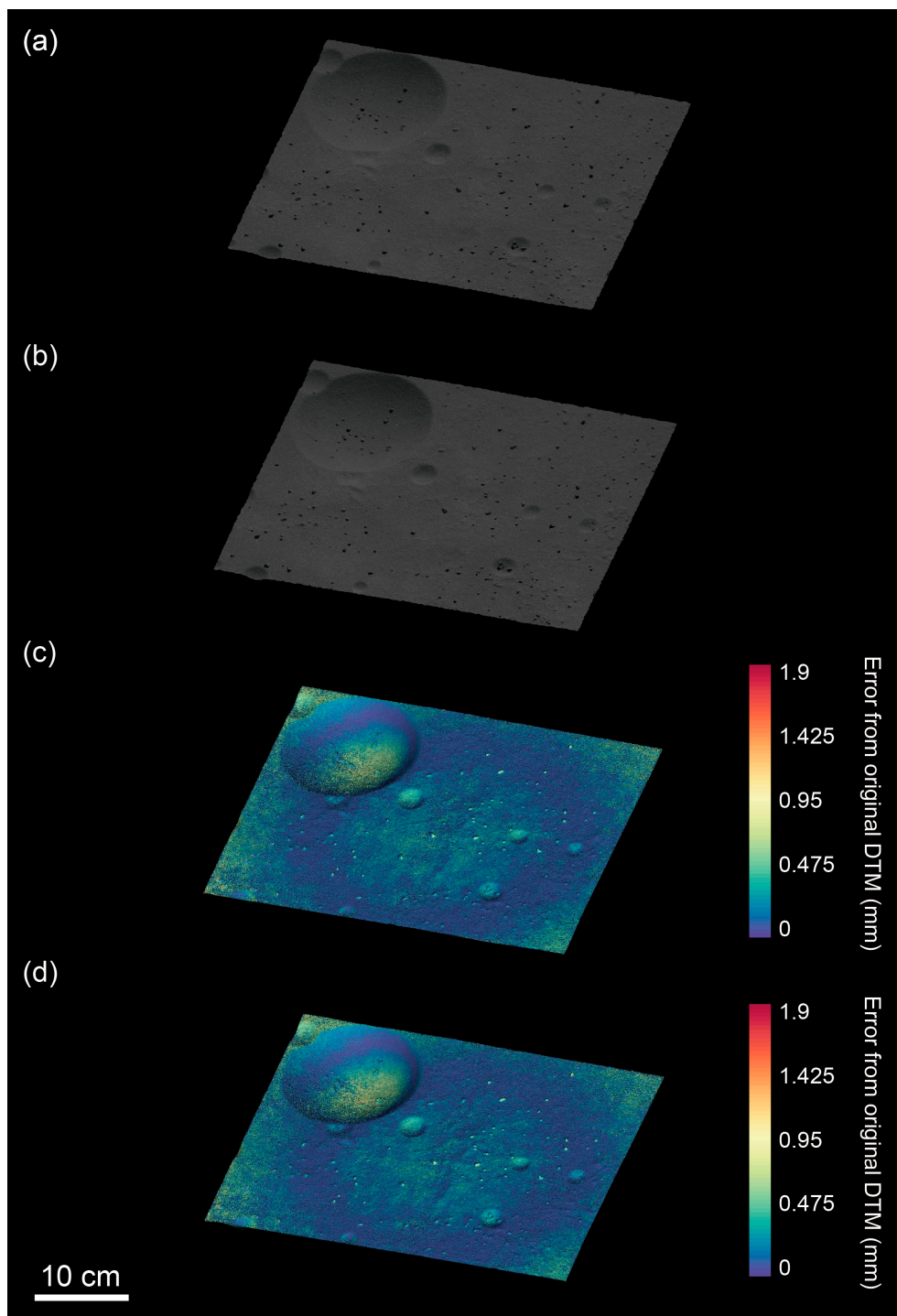


**Figure 9.** Compressed models for the smooth surface and their error analysis. The error analysis shows the error of compressed models from the original models. (a) Local DTM generated by using compressed images processed by CCSDS-120 with float-point DWT. The model is composed of 13,074,155 dense points and 9,848,738 meshes. (b) Local DTM generated by using compressed images processed by CCSDS-120 with integer-point DWT. The model is composed of 12,964,085 dense points and 9,902,717 meshes. (c) The error analysis of the model shown in (a). The error of this model is  $0.205 \pm 0.147$  mm, equivalent to the error of  $21.9 \pm 15.7$  cm on Phobos. (d) The error analysis of the model shown in (b). The error of this model is  $0.200 \pm 0.145$  mm, which is equivalent to the error of

$21.4 \pm 15.5$  cm on Phobos. Both analyses show that the compressed models can be generated within 3% errors of the number of dense points and meshes from the original model. Meanwhile, the altitude errors can be smaller than 40 cm on Phobos. As such, 70% compressed images effectively reduce file sizes without losing important scientific information, especially to determine the safe landing sites.

#### 4.2. Implications for the observation in the MMX mission

Given the nominal image resolution from the QSO ( $\sim 12$  cm/pix), the image size of the TENGOO ( $3296 \times 2472$  pixels), and the area of the equatorial region (latitude  $\leq 30^\circ$ ) of Phobos ( $\sim 936$  km<sup>2</sup>), more than  $\sim 3820$  images (with  $>50\%$  overlapping areas in each image for detailed analysis, including DTM reconstruction) are thought necessary to reveal detailed topography on Phobos for landing site selection. Transmitting all of those images would require  $\sim 180$  days ( $\sim 6.0$  months), but such a duration can be shrunk into  $\sim 54$  days ( $\sim 1.8$  months) using the compression ratio of 70%. This timescale is preferable for the landing site selection phase, currently planned to last approximately six months. Even so, downlink time for the TENGOO will be further constrained by several factors such as uplink communications, downlink of other science instruments onboard the MMX spacecraft, and availability of deep-space communication facilities on the ground. The best compression ratio could change if the target images have different parameters, such as image size, bit depth, and brightness/contrast, from other criteria with varying acceptable local DTM errors. Therefore, determining the best compression ratio for each critical phase in future deep space exploration missions may require different or appropriate methods/criteria. This matter could be a topic for future research.

## 5. Conclusions

Low downlink rates can be one of the greatest limiting factors for deep space exploration missions, including the MMX mission. We thus prepared simulated images of Phobos using rough and smooth surfaces in a laboratory. We subsequently compressed those images using the CCSDS-120 with float- and integer-point DWT candidate algorithms that can be used in the MMX mission. The image quality assessment performed by SSIM shows that the difference in the compression performances between the two algorithms is substantially limited. Notably, the loss of image quality can differ depending on the roughness of the surface in images. But such loss of quality remains constrained if we compress images with a compression ratio lower than or equal to 70%.

We further compared the local DTMs generated using compressed and uncompressed images. Our result shows that the models can be generated with altitude errors smaller than 40 cm on Phobos, even if we compress images with a compression ratio of 70%. Thus, we can expect that the compression ratio can be increased as high as 70% in the MMX mission. Using this compression ratio, we can reduce the data volume without losing important scientific information. This approach can be significantly effective in the MMX mission, particularly during the landing site selection phase, which is one of the most crucial parts of this mission.

**Author Contributions:** Conceptualization, Y.S., and H.M.; methodology, Y.S., H.M., and S.K.; software, Y.S.; validation, Y.S., and H.M.; formal analysis, Y.S.; investigation, Y.S., H.M., and S.K.; resources, H.M., and S.K.; data curation, Y.S., H.M., and S.K.; writing—original draft preparation, Y.S., and H.M.; writing—review and editing, Y.S., H.M., and S.K.; visualization, Y.S.; supervision, H.M.; project administration, H.M. All authors have read and agreed to the published version of the manuscript.

**Funding:** This research was funded by JSPS KAKENHI grant JP21J21798 and 23H00279 .

**Data Availability Statement:** The source code for the compression algorithm, CCSDS-120 is available at <http://hyperspectral.unl.edu/download.htm>. The data presented in this study will be openly available in FigShare at 10.6084/m9.figshare.24251320.

**Conflicts of Interest:** The authors declare no conflict of interest. The funders had no role in the design of the study; in the collection, analyses, or interpretation of data; in the writing of the manuscript; or in the decision to publish the results.

## References

1. Saito, J.; Miyamoto, H.; Nakamura, R.; Ishiguro, M.; Michikami, T.; Nakamura, A.M.; Demura, H.; Sasaki, S.; Hirata, N.; Honda, C.; et al. Detailed images of asteroid 25143 Itokawa from Hayabusa. *Science* **2006**, *312*, 1341-1344, doi:10.1126/science.1125722.
2. Watanabe, S.; Tsuda, Y.; Yoshikawa, M.; Tanaka, S.; Saiki, T.; Nakazawa, S. Hayabusa2 Mission Overview. *Space Science Reviews* **2017**, *208*, 3-16, doi:10.1007/s11214-017-0377-1.
3. Glassmeier, K.H.; Boehnhardt, H.; Koschny, D.; Kührt, E.; Richter, I. The ROSETTA Mission: Flying towards the origin of the solar system. *Space Science Reviews* **2007**, *128*, 1-21, doi:10.1007/s11214-006-9140-8.
4. Lauretta, D.S.; Balram-Knutson, S.S.; Beshore, E.; Boynton, W.V.; d'Aubigny, C.D.; DellaGiustina, D.N.; Enos, H.L.; Golish, D.R.; Hergenrother, C.W.; Howell, E.S.; et al. OSIRIS-REx: Sample Return from Asteroid (101955) Bennu. *Space Science Reviews* **2017**, *212*, 925-984, doi:10.1007/s11214-017-0405-1.
5. Lord, P.; Tilley, S.; Oh, D.Y.; Goebel, D.; Polanskey, C.; Snyder, S.; Carr, G.; Collins, S.M.; Lantoine, G.; Landau, D.; et al. Psyche: Journey to a Metal World. In Proceedings of the IEEE Aerospace Conference, Big Sky, MT, Mar 04-11, 2017.
6. Lorenz, R.D.; MacKenzie, S.M.; Neish, C.D.; Gall, A.L.; Turtle, E.P.; Barnes, J.W.; Trainer, M.G.; Werynski, A.; Hedgepeth, J.; Karkoschka, E. Selection and Characteristics of the Dragonfly Landing Site near Selk Crater, Titan. *Planetary Science Journal* **2021**, *2*, 13, doi:10.3847/PSJ/abd08f.
7. Levison, H.F.; Olkin, C.B.; Noll, K.S.; Marchi, S.; Bell, J.; Bierhaus, E.; Binzel, R.; Bottke, W.; Britt, D.; Brown, M.; et al. Lucy Mission to the Trojan Asteroids: Science Goals. *Planetary Science Journal* **2021**, *2*, 13, doi:10.3847/PSJ/abf840.
8. Michel, P.; Koppers, M.; Bagatin, A.C.; Carry, B.; Charnoz, S.; de Leon, J.; Fitzsimmons, A.; Gordo, P.; Green, S.F.; Herique, A.; et al. The ESA Hera Mission: Detailed Characterization of the DART Impact Outcome and of the Binary Asteroid (65803) Didymos. *Planetary Science Journal* **2022**, *3*, 21, doi:10.3847/PSJ/ac6f52.
9. Kuramoto, K.; Kawakatsu, Y.; Fujimoto, M.; Araya, A.; Barucci, M.A.; Genda, H.; Hirata, N.; Ikeda, H.; Imamura, T.; Helbert, J.; et al. Martian moons exploration MMX: sample return mission to Phobos elucidating formation processes of habitable planets. *Earth Planets and Space* **2022**, *74*, 31, doi:10.1186/s40623-021-01545-7.
10. Pollack, J.B.; Veverka, J.; Pang, K.; Colburn, D.; Lane, A.L.; Ajello, J.M. Multicolor observations of Phobos with the Viking Lander cameras: Evidence for a carbonaceous chondritic composition. *Science* **1978**, *199*, 66-69.
11. Hartmann, W.K. Additional Evidence about An Early Intense Flux of C-asteroids and The Origin of Phobos. *Icarus* **1990**, *87*, 236-240, doi:10.1016/0019-1035(90)90033-6.
12. Pajola, M.; Lazzarin, M.; Ore, C.M.D.; Cruikshank, D.P.; Roush, T.L.; Magrin, S.; Bertini, I.; La Forgia, F.; Barbieri, C. Phobos as A D-type Captured Asteroid, Spectral Modeling from 0.25 to 4.0  $\mu\text{m}$ . *Astrophysical Journal* **2013**, *777*, 6, doi:10.1088/0004-637x/777/2/127.
13. Burns, J.A. Contradictory clues as to the origin of the Martian moons. *Mars* **1992**, 1283-1301.
14. Citron, R.I.; Genda, H.; Ida, S. Formation of Phobos and Deimos via a giant impact. *Icarus* **2015**, *252*, 334-338, doi:10.1016/j.icarus.2015.02.011.
15. Craddock, R.A. Are Phobos and Deimos the result of a giant impact? *Icarus* **2011**, *211*, 1150-1161.
16. Hyodo, R.; Genda, H.; Charnoz, S.; Rosenblatt, P. On the Impact Origin of Phobos and Deimos. I. Thermodynamic and Physical Aspects. *Astrophysical Journal* **2017**, *845*, 8, doi:10.3847/1538-4357/aa81c4.
17. Hyodo, R.; Rosenblatt, P.; Genda, H.; Charnoz, S. On the Impact Origin of Phobos and Deimos. II. True Polar Wander and Disk Evolution. *Astrophysical Journal* **2017**, *851*, 9, doi:10.3847/1538-4357/aa9984.
18. Hyodo, R.; Genda, H.; Charnoz, S.; Pignatale, F.C.F.; Rosenblatt, P. On the Impact Origin of Phobos and Deimos. IV. Volatile Depletion. *Astrophysical Journal* **2018**, *860*, 10, doi:10.3847/1538-4357/aac024.
19. Pignatale, F.C.; Charnoz, S.; Rosenblatt, P.; Hyodo, R.; Nakamura, T.; Genda, H. On the Impact Origin of Phobos and Deimos. III. Resulting Composition from Different Impactors. *Astrophysical Journal* **2018**, *853*, 12, doi:10.3847/1538-4357/aaa23e.
20. Nakamura, T.; Ikeda, H.; Kouyama, T.; Nakagawa, H.; Kusano, H.; Senshu, H.; Kameda, S.; Matsumoto, K.; Gonzalez-Franquesa, F.; Ozaki, N.; et al. Science operation plan of Phobos and Deimos from the MMX spacecraft. *Earth Planets and Space* **2021**, *73*, 27, doi:10.1186/s40623-021-01546-6.
21. Willner, K.; Shi, X.; Oberst, J. Phobos' shape and topography models. *Planetary and Space Science* **2014**, *102*, 51-59, doi:10.1016/j.pss.2013.12.006.
22. Hemmi, R.; Miyamoto, H. Morphology and Morphometry of Sub-kilometer Craters on the Nearsides of Phobos and Implications for Regolith Properties. *Transactions of the Japan Society for Aeronautical and Space Sciences* **2020**, *63*, 124-131, doi:10.2322/tjsass.63.124.
23. Basilevsky, A.T.; Lorenz, C.A.; Shingareva, T.V.; Head, J.W.; Ramsley, K.R.; Zubarev, A.E. The surface geology and geomorphology of Phobos. *Planetary and Space Science* **2014**, *102*, 95-118, doi:10.1016/j.pss.2014.04.013.

24. Karachevtseva, I.P.; Oberst, J.; Zubarev, A.E.; Nadezhkina, I.E.; Kokhanov, A.A.; Garov, A.S.; Uchaev, D.V.; Malinnikov, V.A.; Klimkin, N.D. The Phobos information system. *Planetary and Space Science* **2014**, *102*, 74-85, doi:10.1016/j.pss.2013.12.015.
25. Salamuniccar, G.; Loncaric, S.; Pina, P.; Bandeira, L.; Saraiva, J. Integrated Crater Detection Algorithm and Systematic Cataloging of Phobos Craters. *Proceedings of the 7th International Symposium on Image and Signal Processing and Analysis (Isipa 2011)* **2011**, 591-596.
26. Salamuniccar, G.; Loncaric, S.; Pina, P.; Bandeira, L.; Saraiva, J. Integrated method for crater detection from topography and optical images and the new PH9224GT catalogue of Phobos impact craters. *Advances in Space Research* **2014**, *53*, 1798-1809, doi:10.1016/j.asr.2013.11.006.
27. Schmedemann, N.; Michael, G.G.; Ivanov, B.A.; Murray, J.B.; Neukum, G. The age of Phobos and its largest crater, Stickney. *Planetary and Space Science* **2014**, *102*, 152-163, doi:10.1016/j.pss.2014.04.009.
28. Thomas, P.C.; Veverka, J.; Sullivan, R.; Simonelli, D.P.; Malin, M.C.; Caplinger, M.; Hartmann, W.K.; James, P.B. Phobos: Regolith and ejecta blocks investigated with Mars Orbiter Camera images. *Journal of Geophysical Research-Planets* **2000**, *105*, 15091-15106, doi:10.1029/1999je001204.
29. Murray, J.B.; Heggie, D.C. Character and origin of Phobos' grooves. *Planetary and Space Science* **2014**, *102*, 119-143, doi:10.1016/j.pss.2014.03.001.
30. Wilson, L.; Head, J.W. Groove formation on Phobos: Testing the Stickney ejecta emplacement model for a subset of the groove population. *Planetary and Space Science* **2015**, *105*, 26-42, doi:10.1016/j.pss.2014.11.001.
31. Thomas, P.; Veverka, J.; Bloom, A.; Duxbury, T. Grooves on Phobos - Their Distribution, Morphology and Possible Origin. *Journal of Geophysical Research* **1979**, *84*, 8457-8477, doi:10.1029/JB084iB14p08457.
32. Andert, T.P.; Rosenblatt, P.; Patzold, M.; Hausler, B.; Dehant, V.; Tyler, G.L.; Marty, J.C. Precise mass determination and the nature of Phobos. *Geophysical Research Letters* **2010**, *37*, 4, doi:10.1029/2009gl041829.
33. Ballouz, R.L.; Walsh, K.J.; Sanchez, P.; Holsapple, K.A.; Michel, P.; Scheeres, D.J.; Zhang, Y.; Richardson, D.C.; Barnouin, O.S.; Nolan, M.C.; et al. Modified granular impact force laws for the OSIRIS-REx touchdown on the surface of asteroid (101955) Bennu. *Monthly Notices of the Royal Astronomical Society* **2021**, *507*, 5087-5105, doi:10.1093/mnras/stab2365.
34. Terui, F.; Ogawa, N.; Ono, G.; Yasuda, S.; Masuda, T.; Matsushima, K.; Saiki, T.; Tsuda, Y. Guidance, navigation, and control of Hayabusa2 touchdown operations. *Astrodynamics* **2020**, *4*, 393-409, doi:10.1007/s42064-020-0086-5.
35. Walsh, K.J.; Ballouz, R.L.; Jawin, E.R.; Avdellidou, C.; Barnouin, O.S.; Bennett, C.A.; Bierhaus, E.B.; Bos, B.J.; Cambioni, S.; Connolly, H.C.; et al. Near-zero cohesion and loose packing of Bennu's near subsurface revealed by spacecraft contact. *Science Advances* **2022**, *8*, eabm6229, doi:10.1126/sciadv.abm6229.
36. Yano, H.; Kubota, T.; Miyamoto, H.; Okada, T.; Scheeres, D.; Takagi, Y.; Yoshida, K.; Abe, M.; Abe, S.; Barnouin-Jha, O.; et al. Touchdown of the Hayabusa spacecraft at the Muses Sea on Itokawa. *Science* **2006**, *312*, 1350-1353, doi:10.1126/science.1126164.
37. Yoshikawa, K.; Sawada, H.; Kikuchi, S.; Ogawa, N.; Mimasu, Y.; Ono, G.; Takei, Y.; Terui, F.; Saiki, T.; Yasuda, S.; et al. Modeling and analysis of Hayabusa2 touchdown. *Astrodynamics* **2020**, *4*, 119-135, doi:10.1007/s42064-020-0073-x.
38. Takemura, T.; Miyamoto, H.; Hemmi, R.; Niihara, T.; Michel, P. Small-scale topographic irregularities on Phobos: image and numerical analyses for MMX mission. *Earth Planets and Space* **2021**, *73*, 14, doi:10.1186/s40623-021-01463-8.
39. Pollack, J.B.; Born, G.H.; Smith, B.A.; Veverka, J.; Sagan, C.; Duxbury, T.C.; Milton, D.J.; Hartmann, W.K.; Noland, M. Mariner 9 Television Observations of Phobos and Deimos. *Icarus* **1972**, *17*, 394-&, doi:10.1016/0019-1035(72)90007-3.
40. Veverka, J.; Duxbury, T.C. Viking observations of Phobos and Deimos: Preliminary results. *Journal of Geophysical Research* **1977**, *82*, 4213-4223.
41. Witasse, O.; Duxbury, T.; Chicarro, A.; Altobelli, N.; Andert, T.; Aronica, A.; Barabash, S.; Bertaux, J.L.; Bibring, J.P.; Cardesin-Moinelo, A.; et al. Mars Express investigations of Phobos and Deimos. *Planetary and Space Science* **2014**, *102*, 18-34, doi:10.1016/j.pss.2013.08.002.
42. Thomas, N.; Stelter, R.; Ivanov, A.; Bridges, N.T.; Herkenhoff, K.E.; McEwen, A.S. Spectral heterogeneity on Phobos and Deimos: HiRISE observations and comparisons to Mars Pathfinder results. *Planetary and Space Science* **2011**, *59*, 1281-1292, doi:10.1016/j.pss.2010.04.018.
43. Amiri, H.E.S.; Brain, D.; Sharaf, O.; Withnell, P.; McGrath, M.; Alloghani, M.; Al Awadhi, M.; Al Dhafri, S.; Al Hamadi, O.; Al Matroushi, H.; et al. The Emirates Mars Mission. *Space Science Reviews* **2022**, *218*, 46, doi:10.1007/s11214-021-00868-x.
44. Kameda, S.; Ozaki, M.; Enya, K.; Fuse, R.; Kouyama, T.; Sakatani, N.; Suzuki, H.; Osada, N.; Kato, H.; Miyamoto, H.; et al. Design of telescopic nadir imager for geomorphology (TENGOO) and observation of surface reflectance by optical chromatic imager (OROCHI) for the Martian Moons Exploration (MMX). *Earth Planets and Space* **2021**, *73*, 14, doi:10.1186/s40623-021-01462-9.

45. Ishiguro, M.; Nakamura, R.; Tholen, D.J.; Hirata, N.; Demura, H.; Nemoto, E.; Nakamura, A.M.; Higuchi, Y.; Sogame, A.; Yamamoto, A.; et al. The Hayabusa Spacecraft Asteroid Multi-band Imaging Camera (AMICA). *Icarus* **2010**, *207*, 714-731, doi:10.1016/j.icarus.2009.12.035.
46. Kameda, S.; Suzuki, H.; Takamatsu, T.; Cho, Y.; Yasuda, T.; Yamada, M.; Sawada, H.; Honda, R.; Morota, T.; Honda, C.; et al. Preflight Calibration Test Results for Optical Navigation Camera Telescope (ONC-T) Onboard the Hayabusa2 Spacecraft. *Space Science Reviews* **2017**, *208*, 17-31, doi:10.1007/s11214-015-0227-y.
47. Rizk, B.; d'Aubigny, C.D.; Golish, D.; Fellows, C.; Merrill, C.; Smith, P.; Walker, M.S.; Hendershot, J.E.; Hancock, J.; Bailey, S.H.; et al. OCAMS: The OSIRIS-REx Camera Suite. *Space Science Reviews* **2018**, *214*, 1-55, doi:10.1007/s11214-017-0460-7.
48. Re, C.; Simioni, E.; Cremonese, G.; Roncella, R.; Forlani, G.; Langevin, Y.; Da Deppo, V.; Naletto, G.; Salemi, G. Effects of image compression and illumination on digital terrain models for the stereo camera of the BepiColombo mission. *Planetary and Space Science* **2017**, *136*, 1-14, doi:10.1016/j.pss.2016.10.018.
49. Shimizu, Y.; Kamiyoshihara, H.; Niihara, T.; Miyamoto, H. Experimental Study to Determine the Best Compression Ratio of High-Resolution Images of Small Bodies for the Martian Moons eXploration Mission. *Transactions of the Japan Society for Aeronautical and Space Sciences* **2020**, *63*, 212-221, doi:10.2322/tjsass.63.212.
50. Miyamoto, H.; Niihara, T.; Wada, K.; Ogawa, K.; Senshu, H.; Michel, P.; Kikuchi, H.; Hemmi, R.; Nakamura, T.; Nakamura, A.M.; et al. Surface environment of Phobos and Phobos simulant UTPS. *Earth Planets and Space* **2021**, *73*, 17, doi:10.1186/s40623-021-01406-3.
51. Wang, Z.; Bovik, A.C.; Sheikh, H.R.; Simoncelli, E.P. Image quality assessment: From error visibility to structural similarity. *Ieee Transactions on Image Processing* **2004**, *13*, 600-612, doi:10.1109/tip.2003.819861.
52. McEwen, A.S.; Eliason, E.M.; Bergstrom, J.W.; Bridges, N.T.; Hansen, C.J.; Delamere, W.A.; Grant, J.A.; Gulick, V.C.; Herkenhoff, K.E.; Keszthelyi, L.; et al. Mars Reconnaissance Orbiter's High Resolution Imaging Science Experiment (HiRISE). *Journal of Geophysical Research-Planets* **2007**, *112*, 40, doi:10.1029/2005je002605.
53. Gaskell, R.W.; Barnouin-Jha, O.S.; Scheeres, D.J.; Konopliv, A.S.; Mukai, T.; Abe, S.; Saito, J.; Ishiguro, M.; Kubota, T.; Hashimoto, T.; et al. Characterizing and navigating small bodies with imaging data. *Meteoritics & Planetary Science* **2008**, *43*, 1049-1061, doi:10.1111/j.1945-5100.2008.tb00692.x.
54. Watanabe, S.; Hirabayashi, M.; Hirata, N.; Noguchi, R.; Shimaki, Y.; Ikeda, H.; Tatsumi, E.; Yoshikawa, M.; Kikuchi, S.; Yabuta, H.; et al. Hayabusa2 arrives at the carbonaceous asteroid 162173 Ryugu-A spinning top-shaped rubble pile. *Science* **2019**, *364*, 268-272, doi:10.1126/science.aav8032.

**Disclaimer/Publisher's Note:** The statements, opinions and data contained in all publications are solely those of the individual author(s) and contributor(s) and not of MDPI and/or the editor(s). MDPI and/or the editor(s) disclaim responsibility for any injury to people or property resulting from any ideas, methods, instructions or products referred to in the content.